

Synthesis and toxicity assessment of Fe₃O₄ NPs grafted by ~NH₂-Schiff base as anticancer drug: modeling and proposed molecular mechanism through docking and molecular dynamic simulation

Rahime Eshaghi Malekshah^a, Bahareh Fahimirad^a, Mohammadreza Aallaei^b and Ali Khaleghian^c

^aDepartment of Chemistry, College of Science, Semnan University, Semnan, Iran; ^bDepartment of Chemistry, Faculty of Science, Imam Hossein University, Tehran, Iran; ^cBiochemistry Department, Faculty of Medicine, Semnan University of Medical Sciences, Semnan, Iran

ABSTRACT

Superparamagnetic iron oxide nanoparticles have been synthesized using chain length of (3-amino-propyl) triethoxysilane for cancer therapy. First, we have developed a layer by layer functionalized with grafting 2,4-toluene diisocyanate as a bi-functional covalent linker onto a nano-Fe₃O₄ support. Then, they were characterized by Fourier transform infrared, X-ray powder diffraction, field emission scanning electron microscopy, energy-dispersive X-ray spectroscopy, and VSM techniques. Finally, all nanoparticles with positive or negative surface charges were tested against K562 (myelogenous leukemia cancer) cell lines to demonstrate their therapeutic efficacy by MTT assay test. We found that the higher toxicity of Fe₃O₄@SiO₂@APTS~Schiff base-Cu(II) (IC₅₀: 1000 µg/mL) is due to their stronger *in situ* degradation, with larger intracellular release of iron ions, as compared to surface passivated NPs. For first time, the molecular dynamic simulations of all compounds were carried out afterwards optimizing using MM+, Semi-empirical (AM1) and Ab-initio (STO-3G), Forcite Gemo Opt, Forcite Dynamics, Forcite Energy and CASTEP in Materials studio 2017. The energy (eV), space group, lattice parameters (Å), unit cell parameters (Å), and electron density of the predicted structures were taken from the CASTEP module of Materials Studio. The docking methods were used to predict the DNA binding affinity, ribonucleotide reductase, and topoisomerase II.

ARTICLE HISTORY

Received 2 April 2020
Revised 20 July 2020
Accepted 22 July 2020

KEYWORDS


Synthesis; nanocarrier; MTT assay; computational methods; molecular docking

1. Introduction

Cancer is certainly one of the deadliest diseases in our society and serves as a primary targets in the field of medicinal chemistry. Many different kinds of compounds have been found to be active in restraining the reproduction of cancer cells, and some of them have been used in clinical treatments. Platinating agents, including cisplatin (CDDP), carboplatin (CBDCA), and oxaliplatin (L-OHP) have been widely used in the treatment of a wide spectrum of solid tumors (Abu-Surrah & Kettunen, 2006; Rabik & Dolan, 2007; Hayashi et al., 2016). To reduce side effects of chemotherapy in normal tissues, or decrease in the concentration of drug, the limited spectrum of activity and resistance caused by platinum compounds (Karasawa & Steyger, 2015), on the development of design and synthesis of new non-platinum compounds with potential cytotoxicity have focused in recent years (Yilmaz et al., 2016). In recent decades, inorganic magnetic core-shell nanoparticles (MNPs) as the fascinating area of green chemistry have received considerable attention using environmentally safe reagents and clean synthetic procedures (Dehghani et al., 2013; Esmailpour et al., 2014).

Studies on various nanomaterial have shown that magnetic nanoparticles (MNPs) as an eco-friendly metal oxide have great potential in modern medical applications, including controlled drug and gene delivery systems and improve medical effect of cancer therapy via magnetic hyperthermia, and radiotherapy methodologies (Mancarella et al., 2015; Nigam & Bahadur, 2016; Ranmadugala et al., 2017). Photodynamic therapy (PDT), one of the use of MNPs is mainly taken for cancer diagnosis, selective therapy functions, and anticancer therapy (Nam et al., 2016; Choi et al., 2018). Photodynamic therapy, a major challenge in nanotechnology and nanomedicine, is with minimal side effects (Huang et al., 2011; Yin et al., 2012). Due to properties of the water-soluble photosensitizer MB, Fe₃O₄@mSiO₂(MB)-FA MNPs were synthesized. After treated cells containing different concentrations, the tumor site was exposed to visible light at 650 nm laser. The results demonstrated that system could effectively be in NIR fluorescence imaging (Zhao et al., 2014). Another researches, the MNPs with Chlorin e6 were designed to fluorescence imaging and PDT to diagnose cancer and treat cancer (Huang et al., 2011; Li et al., 2018).

CONTACT Ali Khaleghian  khaleghian.ali@gmail.com, khaleghian@semums.ac.ir  Department of Biochemistry, Faculty of Medicine, Semnan University of Medical Sciences, 5th Km Damghan Road, P.O. Box 3514533, Semnan 3513138111, Iran

 Supplemental data for this article can be accessed [here](#).

© 2020 The Author(s). Published by Informa UK Limited, trading as Taylor & Francis Group.

This is an Open Access article distributed under the terms of the Creative Commons Attribution License (<http://creativecommons.org/licenses/by/4.0/>), which permits unrestricted use, distribution, and reproduction in any medium, provided the original work is properly cited.

Niemirowicz et al. reported the synthesis of core-shell magnetic nanostructures with terminal propyl-amine groups cathelicidin and LL-37 peptide. Then, anticancer activity of MNPs is functionalized by cathelicidin LL-37 against colon cancer culture (DLD-1 cells and HT-29 cells). Results suggest that LL-37 peptide linked to MNPs (MNP@LL-37) have a therapeutic role with a higher rate in treatment and management of cancer compared with treatment using free LL-37 peptide (Niemirowicz et al., 2015). Schiff bases and their metal-based drugs have been great important candidates in coordination chemistry due to their structural similarities with natural biological compounds. They can be synthesized with different metal ions that show desirable activities via azomethine nitrogen atom ($-C=N-$) (Irfan et al., 2020; Revathi et al., 2020). Creation of new Schiff base ligands, as monodentate or multidentate chelating ligands, displays a significant role in antimicrobial activity, antioxidant activity, and cytotoxic effects (Jiang et al., 2020; Tavassoli et al., 2020). Numerous methods have been reported for the preparation of Schiff base (Chen et al., 2014). $Fe_3O_4/SiO_2/APTS$ ($\sim NH_2$) was synthesized and then functionalized by Schiff base complex Cu(II). The results of apoptosis study of Schiff base and complex nanoparticles showed apoptosis percentage of the nanoparticles increased upon increasing the thickness of Fe_3O_4 shell on the magnetite core (Malekshah et al., 2020). In this research, we decided to prepare and characterize Schiff base onto the surface of a novel magnetic nanosystem (iron oxide core) with (3-aminopropyl)triethoxysilane layer (a bridge between the surface of Fe_3O_4 nanoparticles and complex-Schiff base) as a novel method, green and recyclable heterogeneous catalyst (Scheme 1). The molecular dynamic simulations and molecular docking studies of all compounds were performed. In addition, the cytotoxicity properties of compounds were also investigated.

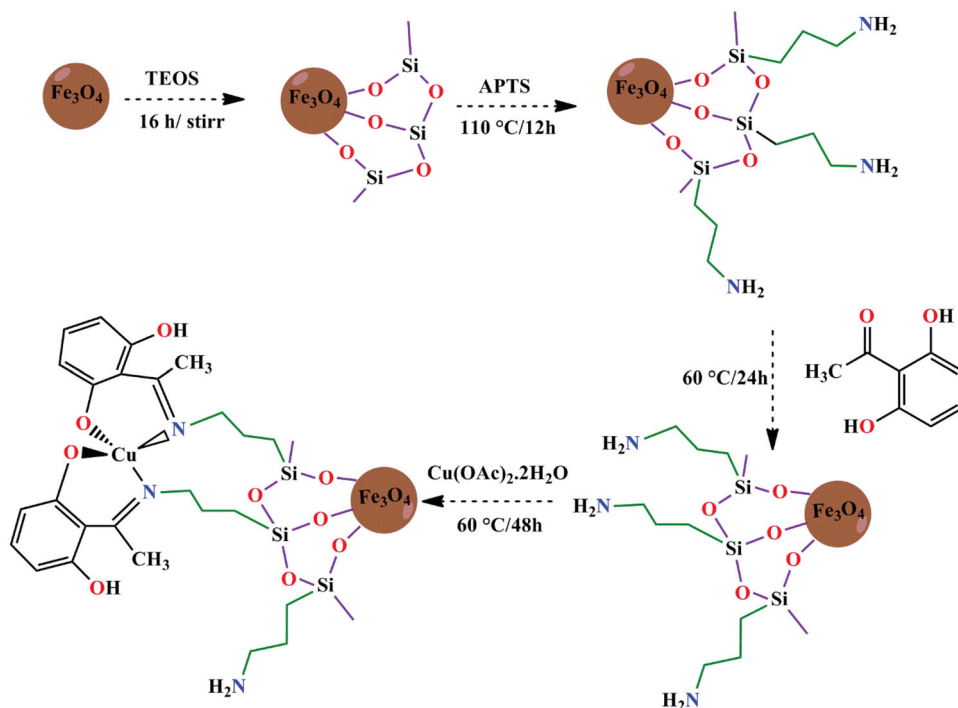
2. Experimental

2.1. Chemicals and instruments

All materials were purchased from Sigma-Aldrich (St. Louis, MO). FT-IR, XRD, SEM, and VSM were recorded on a SHIMADZU UV-1650PC (Kyoto, Japan), a Bruker D8000 (Bremen, Germany) in a scanning range of $2\theta = 10-90^\circ$ and CuK_{α} radiation, HITACHI S-4160 (Chiyoda City, Japan), EDX of the samples was determined using a Philips XL-30 energy-dispersive X-ray spectroscope (Amsterdam, Netherlands) and a vibrating sample magnetometer (VSM) MDKFD, respectively. Cell lines were obtained from National Cell Bank of Iran (NCBI)-Pasteur Institute of Iran (Tehran, Iran). Dulbecco's modified eagle medium-high glucose (DMEM), fetal bovine serum (FBS) and penicillin-streptomycin were obtained from Gibco BRL (Life Technologies, Paisley, Scotland). The culture plates were obtained from Nunc (Roskilde, Denmark). MTT was purchased from Sigma. Chem. Co. (Munich, Germany).

2.1.1. Preparation of the magnetic Fe_3O_4 and $Fe_3O_4@SiO_2$ nanoparticles

Six grams of $FeCl_3 \cdot 6H_2O$ and 2 g $FeCl_2 \cdot 4H_2O$ in 100 mL deionized water were used. After sonicating 20 min, 10 mL of ammoniac solution under a nitrogen atmosphere and temperature at $90^\circ C$ was added dropwise into a mixture solution. After stirring about 1 h, the MNP black precipitate was separated by external magnet. Finally, Fe_3O_4 nanoparticles was washed with the double distilled water and dried at $60^\circ C$ overnight. One gram of Fe_3O_4 was dispersed in 100 mL of the ethanol/ H_2O with ultrasonication. Subsequently, 1.5 mL of ammoniac solution was added and dispersed with ultrasonication for 30 min. In the next step, 10.5 mL TEOS was added into the mixture and stirred for 16 h. The



Scheme 1. The synthesise of $Fe_3O_4@SiO_2@APTS$ NPs functionalized by $\sim NH_2$ -Schiff and its Cu(II).

suspension is filtrated and washed with ethanol and deionized water for three times and dried in oven at 60 °C overnight.

2.1.2. Preparation of $Fe_3O_4@SiO_2@APTS$ core shell

One gram of $Fe_3O_4@SiO_2$ was added in 25 mL toluene and dispersed by ultrasonic. Then, (3-aminopropyl) triethoxysilane (2 mL) was added into the mixture and the solution was refluxed at 110 °C for 12 h. The resulting suspension was collected and washed with ethanol and deionized water for three times and finally dried in a vacuum at 50 °C overnight (Fahimirad et al., 2019).

2.1.3. Preparation of $Fe_3O_4@SiO_2@APTS \sim NH_2$ -Schiff base nanoparticles

For preparation of $Fe_3O_4@SiO_2@APTS \sim NH_2$ -Schiff base nanoparticles, $Fe_3O_4@SiO_2 \sim NH_2$ (0.4 g) was dissolved in 20 mL of methanol. Then, 2,4-dihydroxybenzaldehyde (0.22 g) in methanol (10 mL) added to the solution of $Fe_3O_4@SiO_2@APTS \sim NH_2$ and the resultant mixture was under refluxed at 60 °C for 24 h. The nanoparticles were washed with methanol to remove no reacted species and dried (Roozbahani et al., 2019).

2.1.4. Synthesis of $Fe_3O_4@SiO_2@APTS \sim NH_2$ Schiff base@Cu(II) nanoparticles

Solution of $Cu(OAc)_2 \cdot 2H_2O$ (0.2 g) in methanol was added to $Fe_3O_4@SiO_2@APTS$ -Schiff base (0.2 g, 20 mL MeOH), then the mixture was refluxed at 60 °C for 48 h. The resulting product was separated by filtration and washed with acetone and water (10 mL) and deionized water, then dried in vacuum at 80 °C overnight.

2.2. Biological studies

2.2.1. Preparation of cell culture

The cell lines K562 (a human erythroleukemia cancer) were cultured in DMEM with 10% heat-inactivated FBS (Gibco, Invitrogen, Carlsbad, CA) 104 U/mL penicillin–streptomycin as antibiotics with humidified air containing of 5% CO_2 atmosphere at 37 °C (Heraeus, Hanau, Germany). The cells should have 80–90% confluence before they are harvested and plated for the experiments. The cell lines K562 (a human erythroleukemia cancer) were cultured in minimum essential medium of RPMI 1640 medium with inactivated 10% FBS (Sigma, Munich, Germany), 104 U/mL penicillin–streptomycin as antibiotics (Biosera, Ringmer, UK) in plates and incubated in incubator at 37 °C with 5% CO_2 (Heraeus, Hanau, Germany) (Malekshah et al., 2019).

2.2.2. Assessment of cytotoxicity using MTT assay

The cytotoxicity effect of all compounds was determined in K562 using MTT assay (Malekshah et al., 2018). The cells were seeded at a density of 1×10^3 per well into 96 well tissue culture plates. The amounts of nanoparticles at six different concentrations of 1, 10, 25, 50, 100, and 1000 $\mu g/mL$

were added to the wells after reaching the state of 80% confluence. The plates were incubated in a humidified atmosphere 5% CO_2 . After 48 h, 20 μL of MTT (5 mg/mL) was added to each well and further incubated for 4 h. The medium of the plate was removed and 100 μL of DMSO was added to dissolve the MTT formazan precipitate. The absorbance of samples was determined at 570 nm. The cytotoxicity effect of $Fe_3O_4@SiO_2@APTS \sim$, $Fe_3O_4@SiO_2@APTS \sim$ Schiff base and $Fe_3O_4@SiO_2@APTS \sim$ Schiff base-Cu(II) was determined by MTT method.

2.3. Computational methods

The Fe_3O_4 optimization was done using modules Dmol3 and CASTEP in Materials studio2017. The $Fe_3O_4@SiO_2@APTS \sim$, $Fe_3O_4@SiO_2@APTS \sim$ Schiff base, and $Fe_3O_4@SiO_2@APTS \sim$ Schiff base-Cu(II) were optimized using MM+, Semi-empirical (AM1), and Ab-initio (STO-3G). The modules Forcite Gemo Opt, Forcite Dynamics, Forcite Energy, and CASTEP in Materials studio2017 were used for the final calculation of core–shell linker. The energy (eV), space group, lattice parameters (Å), unit cell parameters (Å), and electron density of the predicted structures were taken from the CASTEP module of Materials Studio.

2.4. Molecular docking of the compounds with DNA duplex of sequence *d* (ACCGACGTCGGT)₂ (PDB ID: 1BNA), ribonucleotide reductase (3hne), and topoisomerase II (PDB ID: 4fm9)

To understand antitumor activity and the binding site of the target-specific region of compounds, we used molecular docking simulation (Malekshah & Khaleghian, 2019). The 3D crystal structures of 1BNA with the sequence, topoisomerase II (PDB ID: 4fm9), anticancer drugs (doxorubicin, mitoxantrone, and trifluridine), ribonucleotide reductase (PDB ID: 3hne1), and triapine were retrieved from RCSB Protein Data Bank and Pubchem. Also, to make cellular membrane, VMD was used by selecting the Extensions → Modeling → Membrane Builder menu item in cellular membrane was built on the *x* and *y* axes and CHARMM topology. In the last, it is converted into pdb format.

The PDB format of synthesized compounds was taken from DMol3 and Castep in Materials studio2017. First of all, the hetero-atoms including water molecules around the duplex were merged using the AutoDock tools, then polar hydrogen atoms, Kollman united atom type charges and Gasteiger partial charges were assigned to the receptor molecule and saved in PDBQT file (Malekshah et al., 2019). All the docking simulations were defined by using a grid box with $74 \times 64 \times 117$ Å points with a grid-point spacing of 0.375 Å for BNA, $126 \times 126 \times 126$ Å with a grid-point spacing of 0.908 Å for Top II, $126 \times 126 \times 126$ Å with a grid-point spacing of 0.980 Å for ribonucleotide reductase and $126 \times 126 \times 126$ Å with a grid-point spacing of 0.602 Å for lipid. The molecular docking using a Lamarckian genetic algorithm method was engaged to study this interaction. The best optimized model having lowest energy was picked

up from the one minimum energy (RMSD = 0.0) from the 100 runs. Then, the interactions and their binding modes with compounds were analyzed using an AutoDock program 1.5.6, UCSF Chimera1.5.3 software, Discovery Studio 2017R2 client from Accelrys and DSVisualizer2.0.

3. Results and discussion

3.1. Infrared spectra of compounds

The stretching vibrations in 3418 and 1618 cm^{-1} are attributed to the O–H stretching and deforming vibrations of

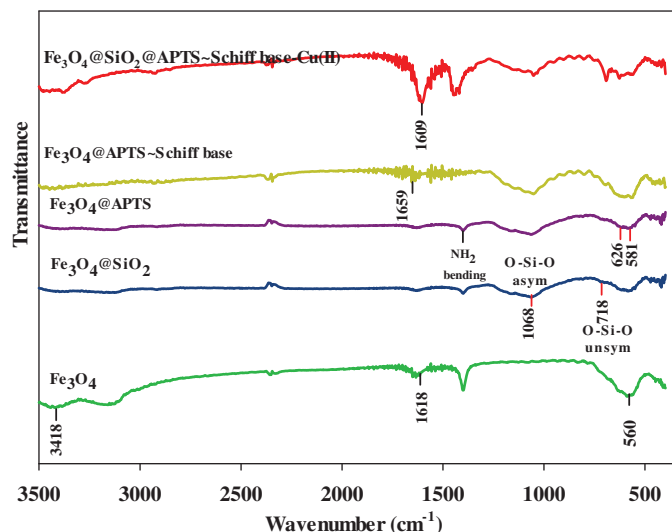


Figure 1. FTIR spectra of bare (a) Fe_3O_4 MNPs; (b) $\text{Fe}_3\text{O}_4@SiO_2$; (c) Fe_3O_4 MNPs treated by APTES; (d) Fe_3O_4 MNPs coated by Schiff base; (e) $\text{Fe}_3\text{O}_4@SiO_2@APTS \sim Schiff \text{ base-Cu(II)}$.

adsorbed water (Figure 1(a)). The absorption around 560 cm^{-1} of Fe_3O_4 is indexed to Fe–O vibration (Fahimirad et al., 2018). In addition, the antisymmetric and symmetric stretching vibration of Si–O–Si and O–Si stretching vibrations are observed at 1068 and 784 cm^{-1} , respectively (Figure 1(b)). Evidently, it indicates that the silica has been successfully coated on the surface of superparamagnetic Fe_3O_4 NPs (Figure 1(b)). Figure 1(c) shows the Fe–O (stretching vibration) at 626 and 581 cm^{-1} , Si–O–Si (asymmetric stretching) in the region 1000–1180 cm^{-1} and C–N (stretching vibration) at 1401 and N–H (bending) at 1639 cm^{-1} , respectively (Esmailpour et al., 2012). In the FT-IR spectrum of $\text{Fe}_3\text{O}_4@SiO_2$ /ligand observed at 1659 cm^{-1} is assigned to the C=N stretching frequency of the newly formed azomethine group and another new band appears around 1509 cm^{-1} which is allocated to the aromatic C=C stretch (Figure 1(d)). Also, O–H stretching band of $\text{Fe}_3\text{O}_4@SiO_2$ /ligand is observed at 3447 cm^{-1} . In addition, the absorption peak at 567 cm^{-1} is assigned for Fe–O stretching vibration in Fe_3O_4 (Tavassoli et al., 2020). The $\nu(\text{C}=\text{N})$ absorption of the Schiff base shift is toward the lower frequency in complex (1609 cm^{-1}), suggesting the coordination of the nitrogen with the metal (Figure 1(e)). The absorption peak at 563 cm^{-1} belonged to the stretching vibration mode of Fe–O bonds in Fe_3O_4 . The presence of vibration bands in 3380 (O–H stretching), 2870–3100 (CH stretching), 1480–1600 (C=C aromatic ring stretching), and 1491 (CH₂ bending) demonstrates the existence of ligand complex of Cu(II) on $\text{Fe}_3\text{O}_4@SiO_2$ nanoparticles in the spectrum (Figure 1(e)). Also, the antisymmetric and symmetric stretching vibrations of Si–O–Si bond in oxygen–silica tetrahedron are observed at 1055 and 814 cm^{-1} , respectively (Kohler et al., 2005).

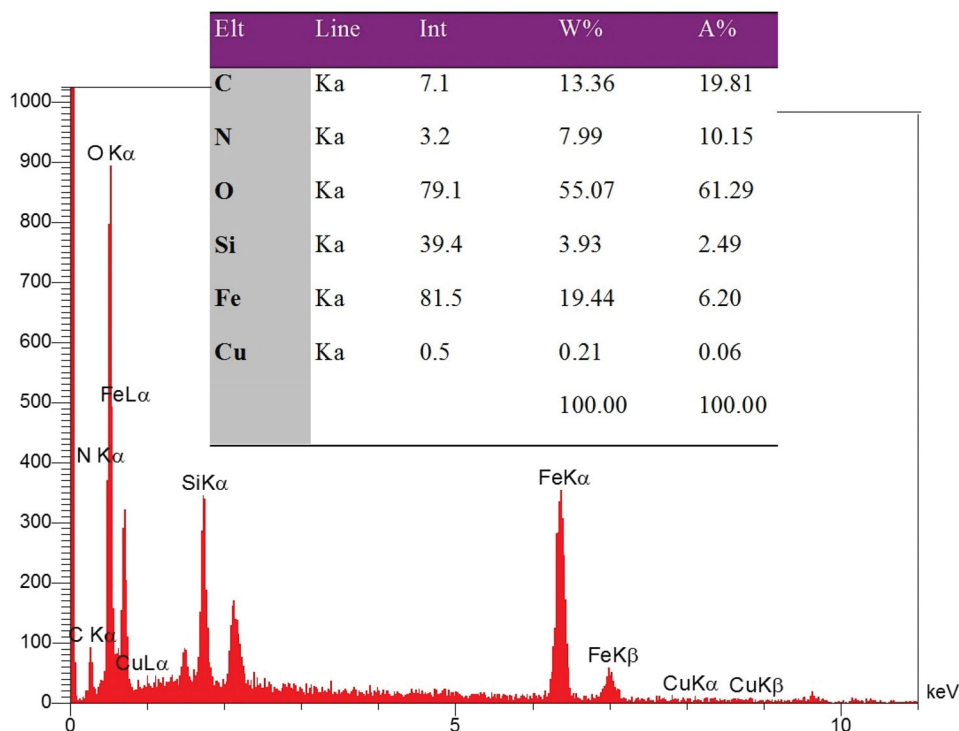


Figure 2. EDX spectra obtained for $\text{Fe}_3\text{O}_4@SiO_2@APTS \sim Schiff \text{ base-Cu(II)}$ nanoparticles.

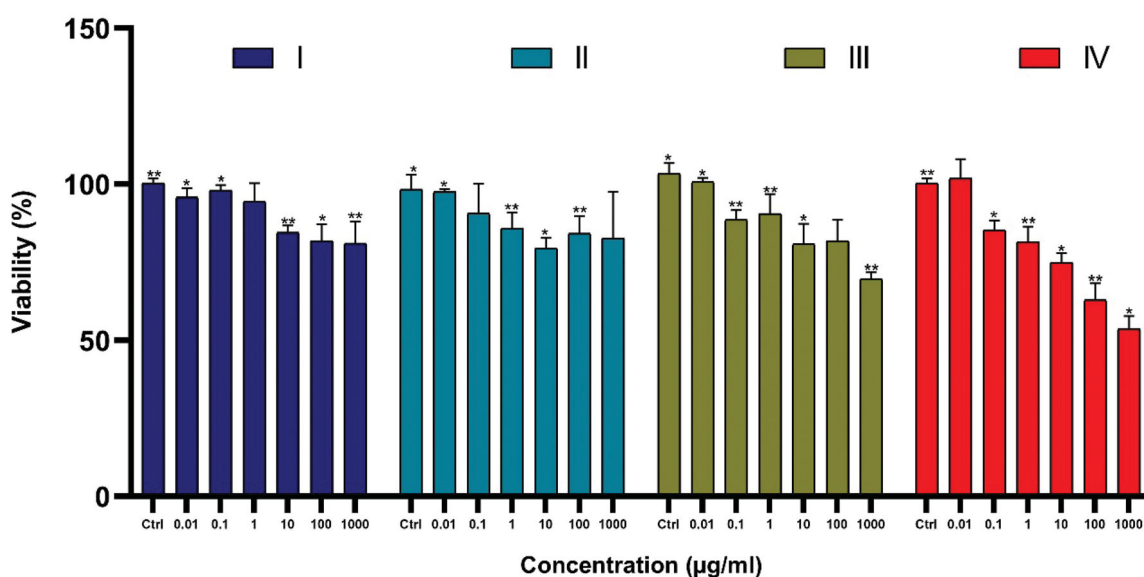


Figure 3. The anti-growth effect after the treatment with varying doses of $\text{Fe}_3\text{O}_4\text{@SiO}_2\text{@APTS}$ (A); $\text{Fe}_3\text{O}_4\text{@SiO}_2\text{@APTS} \sim \text{Schiff base}$ (B); $\text{APTS} \sim \text{Schiff base-Cu(II)}$ (C) on K562 cell lines by the MTT. Data were normalized as a percentage of values of the control (* $p < .05$ and ** $p < .01$).

Table 1. CSP results showing list of unique crystal structures ranked on the basis of the calculated lattice energy and density.

Compound	Fe_3O_4	$\text{Fe}_3\text{O}_4\text{@SiO}_2$	$\text{Fe}_3\text{O}_4\text{@SiO}_2\text{@APTS}$	$\text{Fe}_3\text{O}_4\text{@SiO}_2\text{@APTS} \sim \text{Schiff base}$	$\text{Fe}_3\text{O}_4\text{@SiO}_2\text{@APTS} \sim \text{Schiff base-Cu(II)}$
Crystal system	Rhombohedral	Rhombohedral	Rhombohedral	Rhombohedral	Rhombohedral
Space group	<i>P</i> 1	<i>P</i> 1	<i>P</i> 1	<i>P</i> 1	<i>P</i> 1
<i>a</i> (Å)	6.034	9.025	8.466	9.771	9.973
<i>b</i> (Å)	6.034	9.025	8.466	9.771	9.973
<i>c</i> (Å)	6.034	9.025	8.466	9.771	9.973
α (°)	60.00	90.000	90.000	90.000	90.000
β (°)	60.00	90.000	90.000	90.000	90.000
γ (°)	60.00	90.000	90.000	90.000	90.000
Cell volume	–	735.092	606.957	933.148	992.22
Final energy	–8688.084 eV	–11752.099	–12044.134 eV	–16508.423 eV	–18154.089 eV

3.2. XRD spectra

The crystalline or amorphous structure of compounds was determined by XRD analysis. Therefore, the XRD analysis was taken from samples of $\text{Fe}_3\text{O}_4\text{@SiO}_2$ and $\text{Fe}_3\text{O}_4\text{@SiO}_2\text{@APTS} \sim \text{Schiff base-Cu(II)}$ (Supplementary Figure 1). In two Figure 15. a and 15.b, peaks in $2\theta = 30.1, 34.7, 42.3, 56.2, 57.1,$ and 62.5° can be seen that are in agreement with Fe_3O_4 nanostructures JCPDS no. 19-0629¹⁵. Also, given that the silica and Schiff base complex structures are amorphous, it is expected to be observed broad peak at $2\theta = 20\text{--}30^\circ$. Figure 15.b clearly shows the broad peak at $2\theta = 20\text{--}30^\circ$ that can confirm an amorphous silica shell and organic components in the synthesized structure.

3.3. VSM

The magnetic properties of synthesized sample are analysed by VSM at room temperature. Consequently, in order to obtain the magnetic strength $\text{Fe}_3\text{O}_4\text{@SiO}_2$ and $\text{Fe}_3\text{O}_4\text{@SiO}_2\text{@APTS} \sim \text{Schiff base-Cu(II)}$, the analysis was performed and based on the results in Figure 3, the maximum saturation magnetization (*M*_s) values for Fe_3O_4 and $\text{Fe}_3\text{O}_4\text{@SiO}_2\text{@}$

$\text{APTS} \sim \text{Schiff base-Cu(II)}$ were obtained at 61.60 and 36.23, respectively. According to the results presented in the Supplementary Figure 2, after the surface modification of Fe_3O_4 by $\text{SiO}_2\text{@APTS} \sim \text{Schiff base-Cu(II)}$, the maximum saturation magnetization decreased that it indicates the formation of $\text{SiO}_2\text{@APTS} \sim \text{Schiff base-Cu(II)}$ crust on the Fe_3O_4 core. Finally, $\text{Fe}_3\text{O}_4\text{@SiO}_2\text{@APTS} \sim \text{Schiff base-Cu(II)}$ can be separated easily by using an applied magnetic field.

3.4. SEM and EDX

The FE-SEM images could indicate the distribution of the particles and particle size in synthesizes samples. Therefore, FE-SEM was taken from $\text{Fe}_3\text{O}_4\text{@SiO}_2$ and $\text{Fe}_3\text{O}_4\text{@SiO}_2\text{@APTS} \sim \text{Schiff base-Cu(II)}$ nanoparticles. Supplementary Figure 3 shows a good distribution of the $\text{Fe}_3\text{O}_4\text{@SiO}_2$ particles, indicating a lack of agglomeration in the synthesized $\text{Fe}_3\text{O}_4\text{@SiO}_2$. Also, after modifying of the $\text{Fe}_3\text{O}_4\text{@SiO}_2$ surface by $\text{APTS} \sim \text{Schiff base-Cu(II)}$ nanoparticles, it can be resulted that morphology of nanoparticles has not been changed and the particles are completely dispersed and uniformed. Also, the nanostructures in Supplementary Figures 3.1a and 3.1b have a particle size ~ 20 and about 25 nm, for $\text{Fe}_3\text{O}_4\text{@SiO}_2$

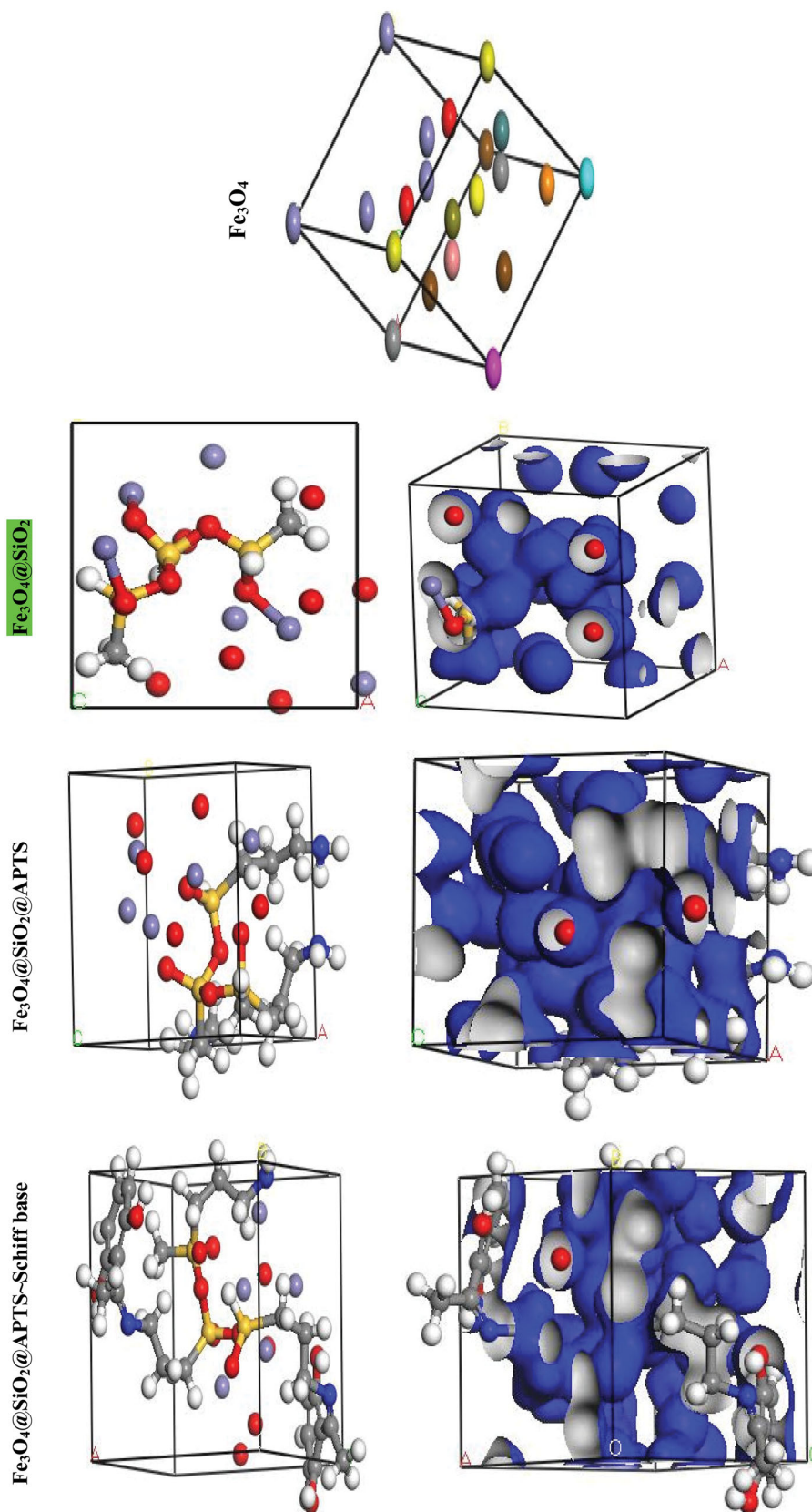


Figure 4. Perspective view and electron density of the optimized nano-particles.

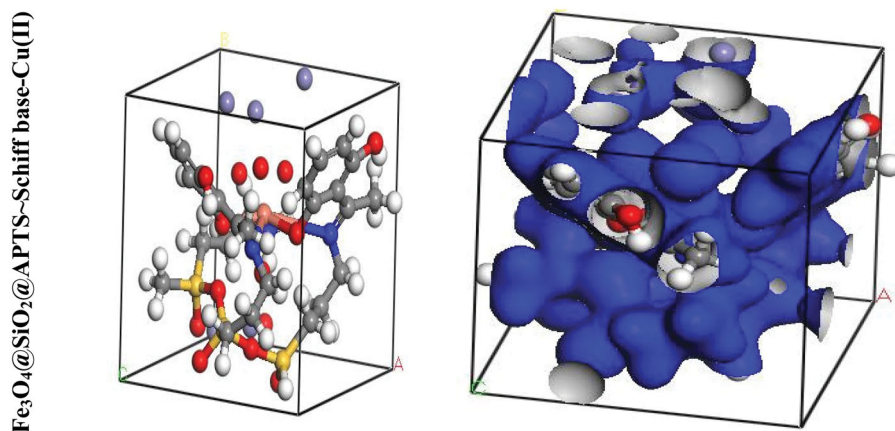


Figure 4. Continued.

and $\text{Fe}_3\text{O}_4@ \text{SiO}_2@ \text{APTS} \sim \text{Schiff base-Cu(II)}$ nanoparticles, respectively. Also, the EDX spectra in Figure 2, conform element of Fe, C, N, Si, and Cu. These results confirm the accuracy of the synthesized sample.

3.5. TEM analysis

Supplementary Figure 4 shows the spherical morphology of the nanocomposite. These were taken from different parts of the sample (Supplementary Figure 4). According to the figure, the particles are well dispersed and the core-shell structure is clearly marked. In this figure, the core of the nanoparticles (Fe_3O_4) is dark regions and the shell structure ($\text{SiO}_2@ \text{APTS} \sim \text{Schiff base-Cu(II)}$) is the lighter regions represent. Also, the figures clearly show the uniformity of the particle size of the nanoparticles. According to these images, the average particle size is approximately 25 nm, which is in agreement with SAM images.

4. Biological assay

4.1. Assessment of cytotoxicity using MTT assay

The cytotoxicity/viability of compounds was examined by conventional MTT assay in K562 cell lines and the results are shown in Figure 3. Our results indicated that the anti-cancer effects of the nanoparticles increased upon increasing the thickness of Fe_3O_4 shell on the magnetite core $\text{Fe}_3\text{O}_4@ \text{SiO}_2@ \text{APTS} \sim \text{Schiff base-Cu(II)} > \text{Fe}_3\text{O}_4@ \text{SiO}_2@ \text{APTS} \sim \text{Schiff base} > \text{Fe}_3\text{O}_4@ \text{SiO}_2@ \text{APTS} > \text{Fe}_3\text{O}_4@ \text{SiO}_2$. Also, the results show that toxicity of nanoparticles is dose dependent and prevent the cell growth and viability with increase in dose.

5. Simulation methods

5.1. Crystal structure prediction (CSP)

We were carried out by NVT (constant particle number, constant volume, and constant temperature) and NPT (constant particle number, constant temperature, and constant pressure) 15 ns in the time and ensemble atomic simulation on

compounds. Details about the data collection and figures of electron density of the optimized compounds are illustrated in Table 1 and Figure 4. The structures of all compounds crystallize in the *Rhombohedral* system with *P1* space groups. The structure of $\text{Fe}_3\text{O}_4@ \text{SiO}_2@ \text{APTS} \sim \text{Schiff base-Cu(II)}$ is tetrahedral with cell volume 992.22 \AA^3 . Cell volume of $\text{Fe}_3\text{O}_4@ \text{SiO}_2$, $\text{Fe}_3\text{O}_4@ \text{SiO}_2@ \text{APTS}$, $\text{Fe}_3\text{O}_4@ \text{SiO}_2@ \text{APTS} \sim \text{Schiff base}$ is 735.092 , 606.957 , and 933.148 \AA^3 , respectively. This compound showed weak π - π stacking and hydrogens interactions between neighboring atoms (Supplementary Fig. 5), in addition, there is no π - π stacking and hydrogen interactions between neighboring atoms and cell data were estimated for $\text{Fe}_3\text{O}_4@ \text{SiO}_2$. The calculated frontier orbital density distributions of all nanoparticles are shown in Figure 4. The electrophilic and nucleophilic segments can be characterized by the levels of electron density observing in the different regions of our compound. The electron charge distributions of the HOMO and LUMO are plotted in Supplementary Figure 6. The HOMO and LUMO energies of $\text{Fe}_3\text{O}_4@ \text{SiO}_2$ are -20.00 and $+1.462 \text{ eV}$, respectively. The HOMOs are largely localized on the Si of silica, while the LUMOs are localized on O of Si and Fe. The HOMO and LUMO energies of $\text{Fe}_3\text{O}_4@ \text{SiO}_2@ \text{APTS}$ are -19.83 and $+5.808 \text{ eV}$, respectively. The HOMOs are largely localized on the OH of silica, while the LUMOs are localized on metal center. The HOMO and LUMO energies of $\text{Fe}_3\text{O}_4@ \text{SiO}_2@ \text{APTS} \sim \text{Schiff base}$ are -22.893 and $+5.877 \text{ eV}$, respectively. The HOMOs and LUMO are largely localized on the (OH of benzene ring and C of benzene ring) and (O of core), respectively. The HOMO and LUMO energies in $\text{Fe}_3\text{O}_4@ \text{SiO}_2@ \text{APTS} \sim \text{Schiff base-Cu(II)}$ display one main band at -23.567 and $+5.779 \text{ eV}$, respectively. The energy band gap, $\Delta E = E_{\text{LUMO}} - E_{\text{HOMO}}$ of $\text{Fe}_3\text{O}_4@ \text{SiO}_2$, $\text{Fe}_3\text{O}_4@ \text{SiO}_2@ \text{APTS}$, $\text{Fe}_3\text{O}_4@ \text{SiO}_2@ \text{APTS} \sim \text{Schiff base}$ and $\text{Fe}_3\text{O}_4@ \text{SiO}_2@ \text{APTS} \sim \text{Schiff base-Cu(II)}$ is 21.46 , 25.63 , 28.77 , and 29.34 eV . Also, based on results of molecular dynamic simulations, the $\text{Fe}_3\text{O}_4@ \text{SiO}_2@ \text{APTS} \sim \text{Schiff base-Cu(II)}$ has four-coordinated metal center with two nitrogen and two oxygen atoms from Schiff bases, resulting in a distorted tetrahedral coordination sphere. CASTEP results explain in Supplementary Figure 7. The values of band gap for $\text{Fe}_3\text{O}_4@ \text{SiO}_2$, $\text{Fe}_3\text{O}_4@ \text{SiO}_2@ \text{APTS}$, $\text{Fe}_3\text{O}_4@ \text{SiO}_2@ \text{APTS} \sim \text{Schiff}$

Table 2. DNA docking results of the compounds (unit: kcal/mol).

Structures	Estimated free energy of binding* (kcal/mol)	Final intermolecular energy (kcal/mol)	vdW + Hbond + desolv energy (kcal/mol)	Electrostatic energy (kcal/mol)	Final total internal energy (kcal/mol)	Torsional free energy (kcal/mol)	Unbound system's energy (kcal/mol)
Mitoxantrone	-10.35	-15.07	-11.84	-3.23	-4.48	+4.77	-4.48
Trifluridine	-5.56	-6.93	-6.85	-0.09	-0.82	+1.37	-0.82
Fe ₃ O ₄ @SiO ₂	-6.46	-12.42	-12.25	-0.17	-3.29	+5.97	-3.29
Fe ₃ O ₄ @SiO ₂ @APTS	-10.85	-11.20	-10.39	-5.67	-1.58	+5.21	-1.58
Fe ₃ O ₄ @SiO ₂ @APTS ~ Schiff base	-7.47	-14.60	-13.30	-1.30	-4.68	+7.13	-4.68
Fe ₃ O ₄ @SiO ₂ @APTS ~ Schiff base-Cu(II)	-7.59	-8.69	-8.45	-0.24	-0.13	+1.10	-0.13

* $\Delta G_{\text{binding}} = \Delta G_{\text{vdW}} + \text{hb} + \text{desolv} + \Delta G_{\text{elec}} + \Delta G_{\text{total}} + \Delta G_{\text{tor}} - \Delta G_{\text{unb}}$

Table 3. Topoisomerase II docking results of the compounds (unit: kcal/mol).

Structures	Estimated free energy of binding* (kcal/mol)	Final intermolecular energy (kcal/mol)	vdW + Hbond + desolv energy (kcal/mol)	Electrostatic energy (kcal/mol)	Final total internal energy (kcal/mol)	Torsional free energy (kcal/mol)	Unbound system's energy (kcal/mol)
Doxorubicin	-6.94	-10.22	-8.37	+1.85	-4.88	+3.28	-4.88
Fe ₃ O ₄ @SiO ₂	-3.69	-9.65	-9.61	+0.05	-1.72	+5.97	-1.72
Fe ₃ O ₄ @SiO ₂ @APTS	-7.70	-14.03	-7.52	-6.51	-2.45	+6.26	-2.45
Fe ₃ O ₄ @SiO ₂ @APTS ~ Schiff base	-3.52	-10.68	-7.78	-2.9	-5.82	+7.16	-5.82
Fe ₃ O ₄ @SiO ₂ @APTS ~ Schiff base-Cu(II)	-7.94	-11.22	-9.09	-2.13	-2.06	+3.28	-2.06

* $\Delta G_{\text{binding}} = \Delta G_{\text{vdW}} + \text{hb} + \text{desolv} + \Delta G_{\text{elec}} + \Delta G_{\text{total}} + \Delta G_{\text{tor}} - \Delta G_{\text{unb}}$

base, and $\text{Fe}_3\text{O}_4@\text{SiO}_2@\text{APTS} \sim \text{Schiff base-Cu(II)}$ were 0.004, 0.027, 0.008, and 0.019 eV, respectively. The band gap of $\text{Fe}_3\text{O}_4@\text{SiO}_2@\text{APTS}$ and $\text{Fe}_3\text{O}_4@\text{SiO}_2@\text{APTS} \sim \text{Schiff base-Cu(II)}$ is higher than $\text{Fe}_3\text{O}_4@\text{SiO}_2$ and $\text{Fe}_3\text{O}_4@\text{SiO}_2@\text{APTS} \sim \text{Schiff base}$. The computational XRD and the experimental XRD are respectively shown in Supplementary Figs. 8 and 1. The optimized computational XRD is similar to that obtained with experimental XRD.

5.2. Molecular docking of the compounds with DNA, topoisomerase II, ribonucleotide reductase, and lipid

The molecular docking studies along with experimental studies could help to explore a compound as a potential drug candidate. The binding free energy values are dominated by the vdW + Hbond + desolv (kcal/mol) negative energy values, suggesting that the binding events of nanoparticles are a spontaneous process. The DNA-binding affinity of the $\text{Fe}_3\text{O}_4@\text{SiO}_2@\text{APTS}$ ($-10.85 \text{ kcal mol}^{-1}$) and mitoxantrone ($-10.35 \text{ kcal mol}^{-1}$) is stronger than the $\text{Fe}_3\text{O}_4@\text{SiO}_2$

($-6.46 \text{ kcal mol}^{-1}$), $\text{Fe}_3\text{O}_4@\text{SiO}_2@\text{APTS} \sim \text{Schiff base}$ ($-7.47 \text{ kcal mol}^{-1}$), $\text{Fe}_3\text{O}_4@\text{SiO}_2@\text{APTS} \sim \text{Schiff base-Cu(II)}$ ($-7.59 \text{ kcal mol}^{-1}$), and trifluridine ($-5.56 \text{ kcal mol}^{-1}$), respectively. The data and figures of compounds are shown in Figure 5 and Table 2. Based on a comparison of among results, all synthesized compounds showed significant affinity to DNA compared to trifluridine (as DNA–drug interaction). Also, compounds and anticancer drugs could bind to the minor groove of DNA.

The docking results of compounds with topoisomerase II are shown in Supplementary Figure 9, listed in Table 3, the values of docking energy are -3.69 , -6.94 , -7.70 , -3.52 , and $-7.94 \text{ kcal mol}^{-1}$ for doxorubicin, $\text{Fe}_3\text{O}_4@\text{SiO}_2$, $\text{Fe}_3\text{O}_4@\text{SiO}_2@\text{APTS}$; $\text{Fe}_3\text{O}_4@\text{SiO}_2@\text{APTS} \sim \text{Schiff base}$ and $\text{Fe}_3\text{O}_4@\text{SiO}_2@\text{APTS} \sim \text{Schiff base-Cu(II)}$ docked to topoisomerase II, respectively. All compounds like doxorubicin binds directly to a DNA, but the binding into the DNA of $\text{Fe}_3\text{O}_4@\text{SiO}_2@\text{APTS}$ and $\text{Fe}_3\text{O}_4@\text{SiO}_2@\text{APTS} \sim \text{Schiff base-Cu(II)}$ are higher than those of $\text{Fe}_3\text{O}_4@\text{SiO}_2@\text{APTS} \sim \text{Schiff base}$ and doxorubicin. 3D pictures of docking conformations revealed

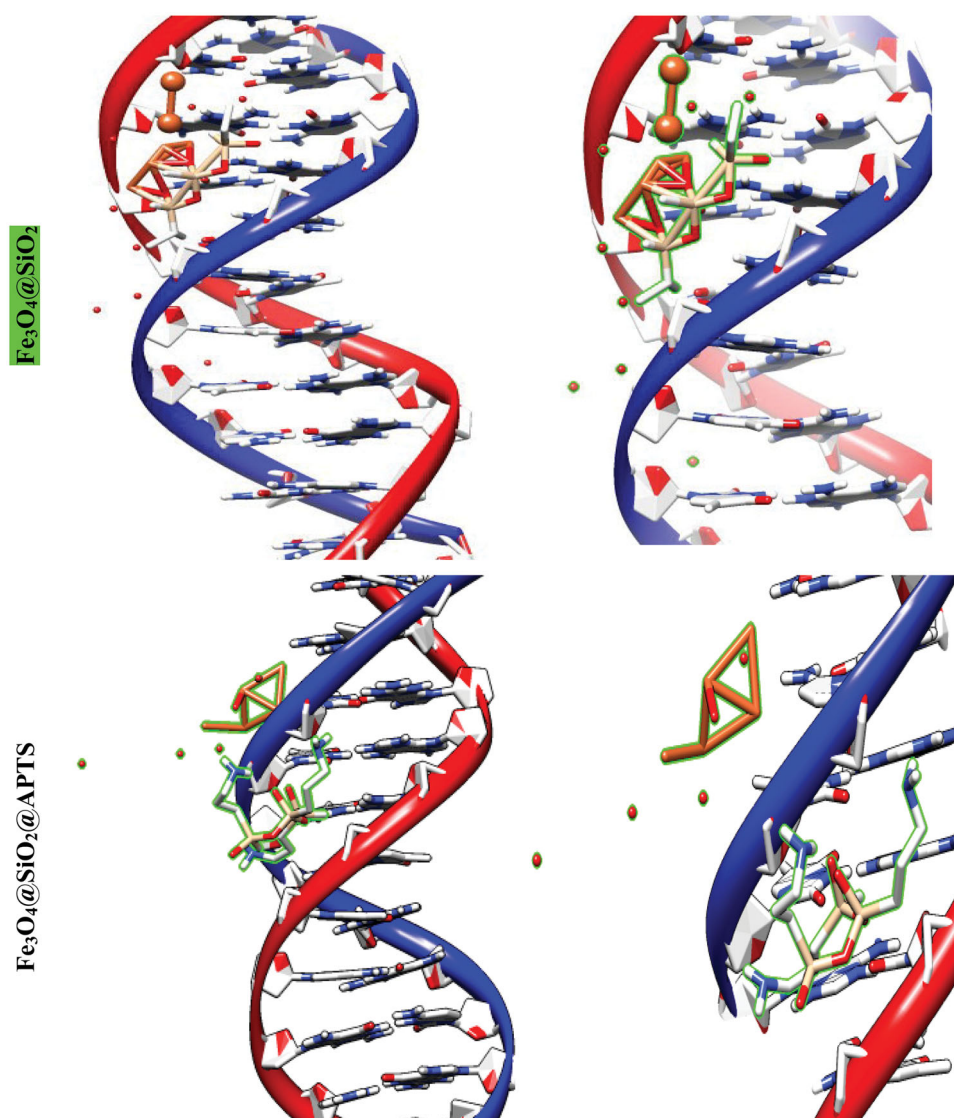


Figure 5. Docking conformation of all synthesized compounds, mitoxantrone and trifluridine with BNA.

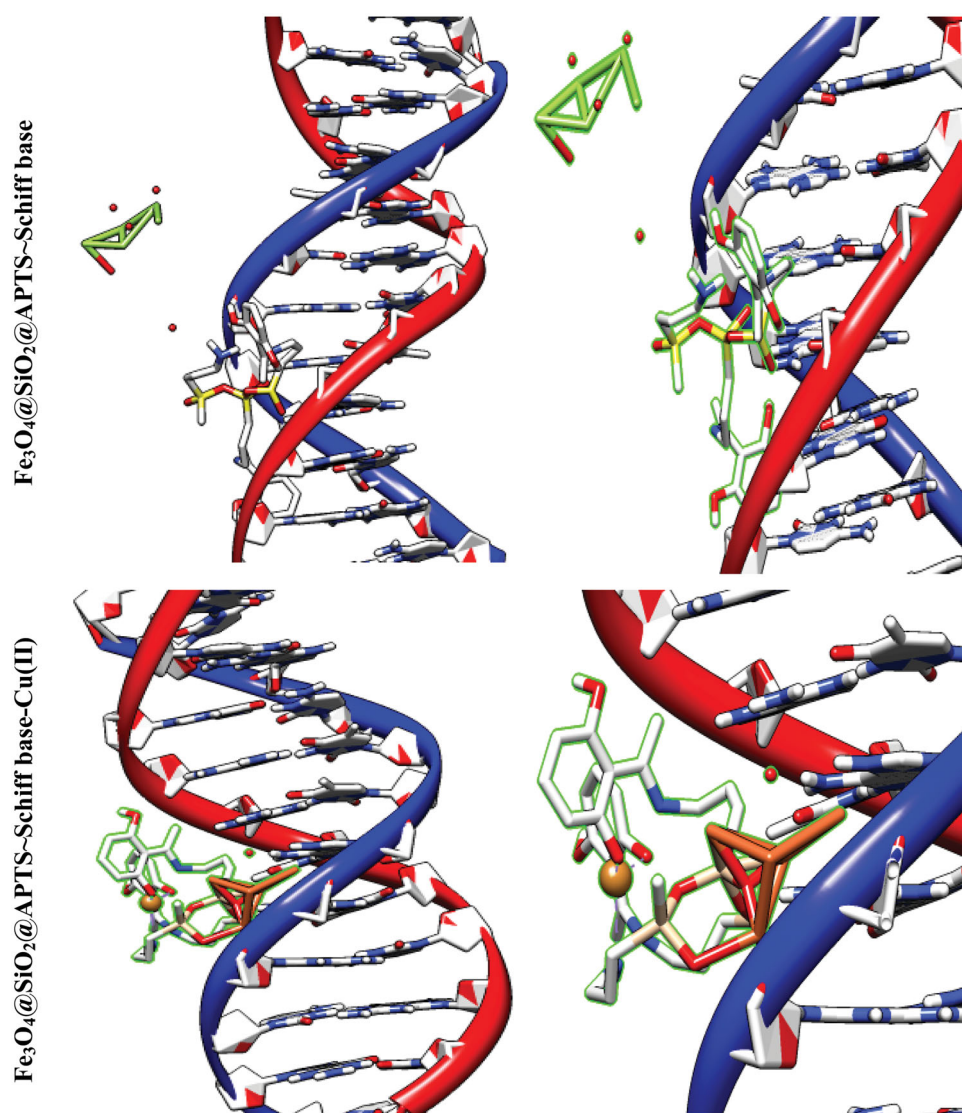


Figure 5. Continued.

that all the compounds were significantly inserted with DNA topoisomerase II via the major groove. $\text{Fe}_3\text{O}_4@SiO_2@APTS \sim Schiff \text{ base-Cu(II)}$ exhibited binding at Glu A:495, Ile A:658, Lys A:655, and Lys A:656 amino acid residue using hydrogen, metal acceptor, alkyl and pi-alkyl bonds. In addition, $\text{Fe}_3\text{O}_4@SiO_2@APTS \sim Schiff \text{ base}$ was docked with Met A:766 amino acid residue using Pi-sulfur, $\text{Fe}_3\text{O}_4@SiO_2@APTS$ docked with Lys A:798 and Ser A:763 using hydrogen, alkyl bonds and $\text{Fe}_3\text{O}_4@SiO_2$ docked with Ser B:244, Lys A:243, ASN B:211, and ASN B:207 using hydrogen.

The docking results of compounds with ribonucleotide reductase are shown in Figure 6 and Tables 4a and 4b. Highest binding affinity of the drug has been identified based on the lowest docking energy. The binding free energy of the $\text{Fe}_3\text{O}_4@SiO_2$, $\text{Fe}_3\text{O}_4@SiO_2@APTS$, $\text{Fe}_3\text{O}_4@SiO_2@APTS \sim Schiff \text{ base}$, $\text{Fe}_3\text{O}_4@SiO_2@APTS \sim Schiff \text{ base-Cu(II)}$, and triapine is dominated by -2.13 , -8.45 , -5.22 , -7.21 ,

and $-3.03 \text{ kcal mol}^{-1}$, respectively. In this simulation, $\text{Fe}_3\text{O}_4@SiO_2$ is located in the pocket formed by Ser B:244, Met B:115, Gly B:214, and Lys B:243 (interaction with the ferric ions), as well as, Asn B:211, and Asn B:207 (interaction with the oxygen ions). $\text{Fe}_3\text{O}_4@SiO_2@APTS$ is located in the pocket formed by Ala B:263 (interaction with one of the ferric ions), Asp B:360, Glu B:361, Asn B:354, and Asp B:225 (three strong hydrogen bonds) and the other hydrophobic non-bonded interactions. Furthermore, $\text{Fe}_3\text{O}_4@SiO_2@APTS \sim Schiff \text{ base}$ is involved in hydrophobic non-bonded interactions (van der Waals bonding and carbon hydrogen bond). The interactions between $\text{Fe}_3\text{O}_4@SiO_2@APTS \sim Schiff \text{ base-Cu(II)}$ and the active sites on the target receptors may be non-covalent interactions like, hydrophobic, and van der Waals interaction. The conserved residues through Pi-sulfur (Met B:115), interaction with the ferric and copper ions (Leu B:157, Arg B:173, and Asn A:266), Glu115, hydrogen bonding (Ser B:154), metal acceptor interaction with one of the ferric

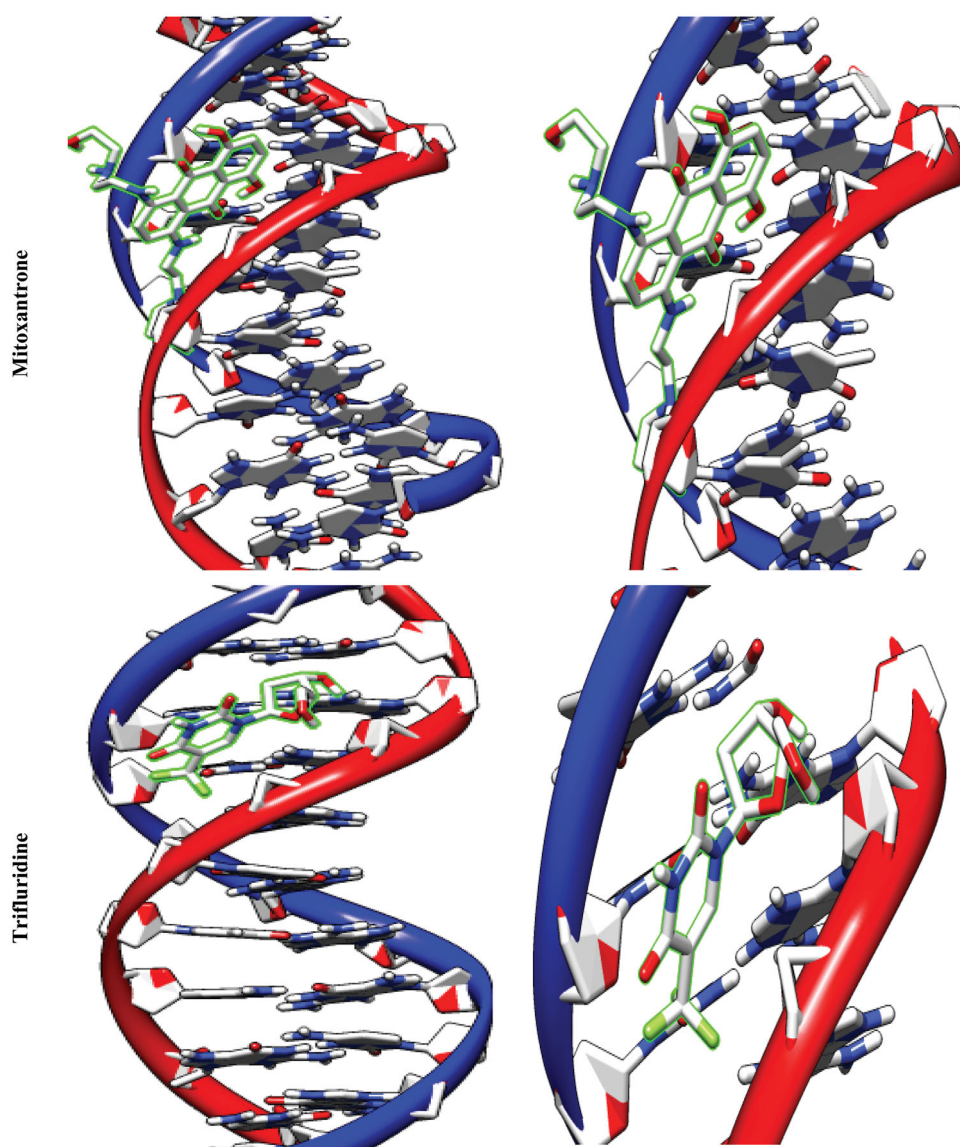


Figure 5. Continued.

ions (Tyr B:155) and van der Waals bonding lie around the pocket. At last, triapine had a strong binding affinity of Pi-sulfur toward Tyr A:568, attractive charge Asp A:569, three hydrogen bond formation with Thr A:574, Tyr A:568, Pro A:575, Lys A:582, and van der Waals bonding.

Phospholipids as bilayer are the major components of biological membranes and consists of an amphipathic (or amphiphilic) including hydrophilic (a polar head group) headgroup and a hydrophobic tail along with one or more cis-double bonds (two hydrophobic hydrocarbon tails). The structures of palmitoylcholine (POPC) were constituted by choline group. By analyzing the energy minimization of each optimized complexation state with POPC, results show the flexible docking algorithm (Cai et al., 2006).

The favorable binding energy minimization of the $\text{Fe}_3\text{O}_4@SiO_2$, $\text{Fe}_3\text{O}_4@SiO_2@APTS$, $\text{Fe}_3\text{O}_4@SiO_2@APTS \sim Schiff$ base, $\text{Fe}_3\text{O}_4@SiO_2@APTS \sim Schiff$ base-Cu(II) with POPC is dominated by -1.66 , -3.31 , -0.57 , and $-5.30 \text{ kcal mol}^{-1}$, respectively. Our results indicated $\text{Fe}_3\text{O}_4@SiO_2@APTS \sim Schiff$

base-Cu(II) $> \text{Fe}_3\text{O}_4@SiO_2@APTS > \text{Fe}_3\text{O}_4@SiO_2 > \text{Fe}_3\text{O}_4@SiO_2@APTS \sim Schiff$ base. From Figure 7, it can be seen that the electrostatic interaction of $\text{Fe}_3\text{O}_4@SiO_2@APTS$ and $\text{Fe}_3\text{O}_4@SiO_2@APTS \sim Schiff$ base-Cu(II) is much stronger than $\text{Fe}_3\text{O}_4@SiO_2@APTS \sim Schiff$ base and $\text{Fe}_3\text{O}_4@SiO_2$. It is mainly due to the strong electrostatic interaction $\text{Fe}_3\text{O}_4@SiO_2@APTS$ and $\text{Fe}_3\text{O}_4@SiO_2@APTS \sim Schiff$ base-Cu(II) with the acyl of polar group on the POPC headgroup. Meanwhile, $\text{Fe}_3\text{O}_4@SiO_2$ and $\text{Fe}_3\text{O}_4@SiO_2@APTS \sim Schiff$ base linked the hydrophobic tail of the phospholipid.

6. Discussion

In summary, the present work illustrates the importance of the molecular dynamic simulations of a series of compounds with grafting 2,4-toluene diisocyanate as a bi-functional covalent linker onto a nano- Fe_3O_4 support for first time. All compounds were characterized by FT-IR, XRD, SEM, EDX, and VSM. The understanding of relationship between iron ions

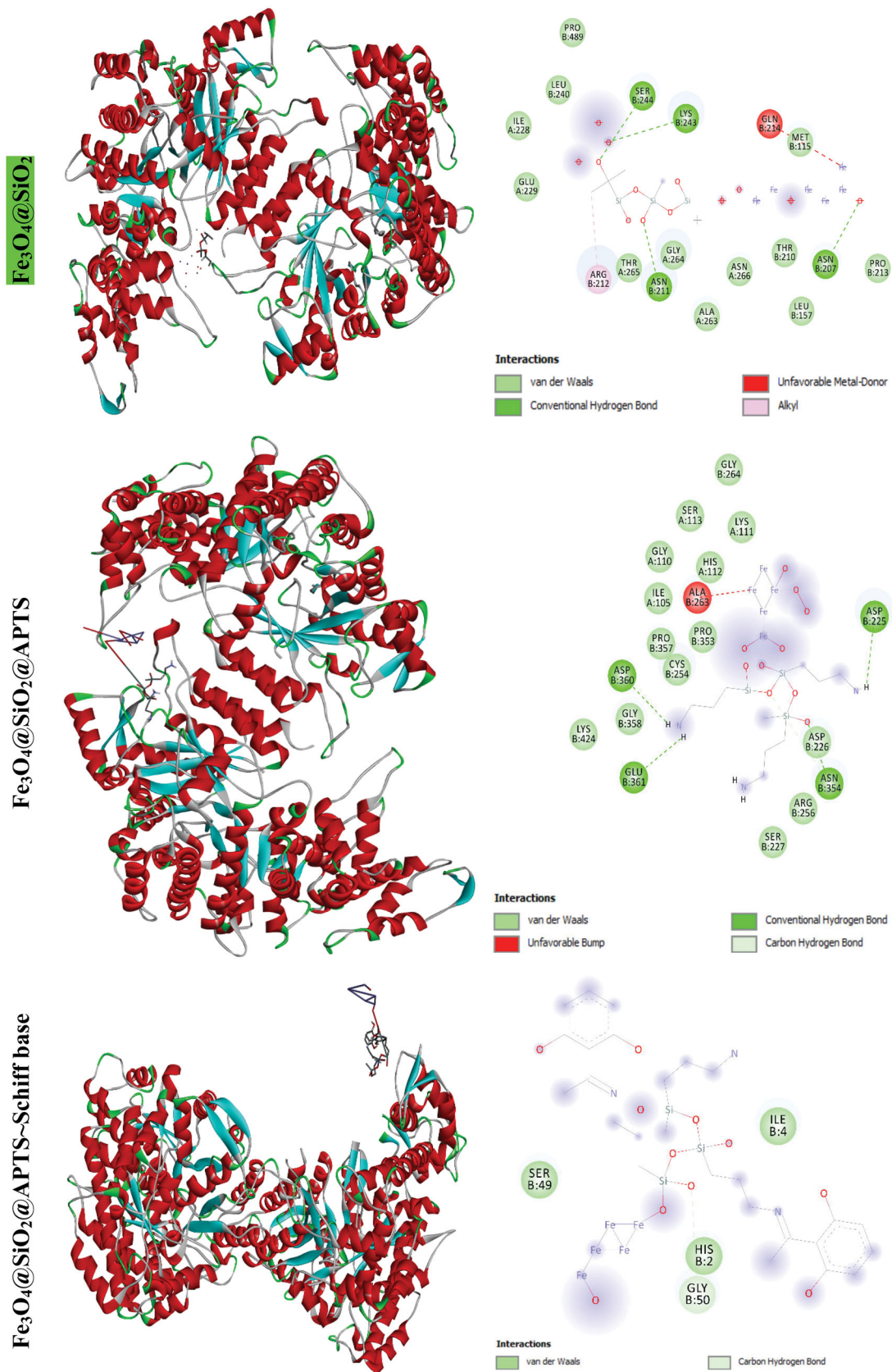


Figure 6. Docking conformation of all synthesized compounds and triapine with ribonucleotide reductase (3hne).

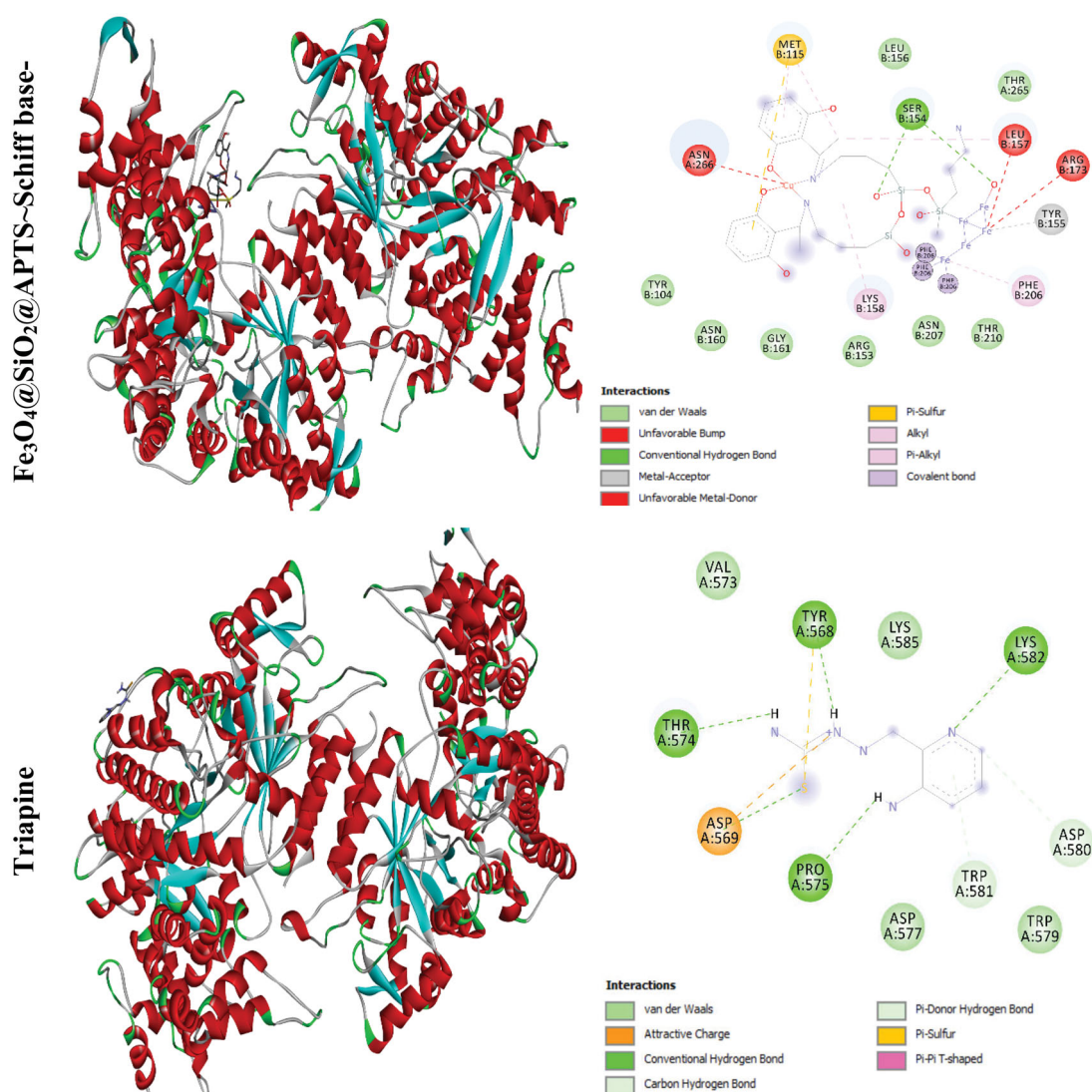


Figure 6. Continued.

release and immunotoxicity of IONPs is important (Singh et al., 2010; Mahon et al., 2012). The IONPs are permeabilized through passive diffusion, clathrin-mediated endocytosis, caveolin-mediated internalization, and other clathrin and caveolin-independent endocytosis (Supplementary Figure 10). The toxicity activities of nanoparticles decreased through increasing nanoparticles chain length and additional protective that created low release of iron ions in intra-cellular space. As a result, additional protection enhances coated iron oxide NPs resistance to the lysosomal acidity, consequently reduction of the iron ions (Fe^{+2}) release. The cell death is caused by interaction between Fe^{+2} with hydrogen peroxide to produce highly reactive hydroxyl radicals and the Fenton reaction in the mitochondria to produce ferric ions (Fe^{3+}) (Halliwell & Gutteridge, 2015). The ROS generation does not counterbalance the action of antioxidant enzymes and may damage biomolecules such as DNA, lipids, and proteins (Palmieri & Sblendorio, 2007; Birben et al., 2012; Abdesselem et al., 2017). Positively charged IONPs generated more ROS compared to neutral and negatively charged IONPs due to

strong electrostatic interaction between the negatively charged cell surface and positively charged IONPs (Cai et al., 2013). Amine-modified IONPs were found to be more lethal *in vitro* tests (Chang et al., 2012; Shen et al., 2012).

Bona et al. synthesized prepared the hydrophilic ligands polyethyleneimine or poly(acrylic acid) on the surface of the NPs and investigated *in vivo*. The results showed bioaccumulation and toxicity with a positively charged surface coating greater than nanoparticles with positively charged surface coating in the fetus (Di Bona et al., 2014).

Fe₃O₄@SiO₂@APTS~Schiff base-Cu(II) demonstrated a higher anticancer properties than Fe₃O₄@SiO₂@APTS~Schiff base, Fe₃O₄@SiO₂@APTS, and Fe₃O₄@SiO₂ (Dunford, 2002; Voinov et al., 2011). Studies on the cytotoxicity properties of these compounds demonstrated lesser toxicity effects at doses of below 0.01 mg/mL (Karlsson et al., 2008; Ankamwar et al., 2010; Malvindi et al., 2014). Due to nano-sized, they might surpass blood-brain barrier (BBB) as protective barrier and damage neural functions and central nervous system (CNS), also can cross nuclear membrane and result mutations

Table 4a. Ribonucleotide reductase docking results of compounds (unit: kcal/mol).

Structures	Estimated free energy of binding* (kcal/mol)	Final intermolecular energy (kcal/mol)	vdW + Hbond + desolv energy (kcal/mol)	Electrostatic energy (kcal/mol)	Final total internal energy (kcal/mol)	Torsional free energy (kcal/mol)	Unbound system's energy (kcal/mol)
Triapine	-3.03	-4.52	-4.45	-0.07	-0.89	+1.49	-0.89
Fe ₃ O ₄ @SiO ₂	-2.13	-8.10	-8.00	-0.10	-3.04	+5.97	-3.04
Fe ₃ O ₄ @SiO ₂ @APTS	-8.45	-14.12	-8.06	-6.06	-1.37	+5.67	-1.37
Fe ₃ O ₄ @SiO ₂ @APTS ~ Schiff base	-5.22	-2.24	-1.81	-0.43	-14.22	+7.46	-14.22
Fe ₃ O ₄ @SiO ₂ @APTS ~ Schiff base-Cu(II)	-7.21	-8.40	-8.38	-0.02	-0.11	+1.19	-0.11

* $\Delta G_{\text{binding}} = \Delta G_{\text{vdW}} + \text{hb} + \text{desolv} + \Delta G_{\text{elec}} + \Delta G_{\text{total}} + \Delta G_{\text{tor}} - \Delta G_{\text{unb}}$

Table 4b. Lipid docking results of compounds (unit: kcal/mol).

Structures	Estimated free energy of binding* (kcal/mol)	Final intermolecular energy (kcal/mol)	vdW + Hbond + desolv energy (kcal/mol)	Electrostatic energy (kcal/mol)	Final total internal energy (kcal/mol)	Torsional free energy (kcal/mol)	Unbound system's energy (kcal/mol)
Fe ₃ O ₄ @SiO ₂	-1.66	-7.62	-7.62	-0.01	-3.17	+5.97	-3.17
Fe ₃ O ₄ @SiO ₂ @APTS	-3.31	-9.87	-8.64	-1.24	-4.04	+6.56	-4.04
Fe ₃ O ₄ @SiO ₂ @APTS ~ Schiff base	-0.57	-10.11	-10.09	-0.02	-7.25	+9.55	-7.25
Fe ₃ O ₄ @SiO ₂ @APTS ~ Schiff base-Cu(II)	-5.30	-9.18	-8.81	-0.37	-1.82	+3.88	-1.82

* $\Delta G_{\text{binding}} = \Delta G_{\text{vdW}} + \text{hb} + \text{desolv} + \Delta G_{\text{elec}} + \Delta G_{\text{total}} + \Delta G_{\text{tor}} - \Delta G_{\text{unb}}$

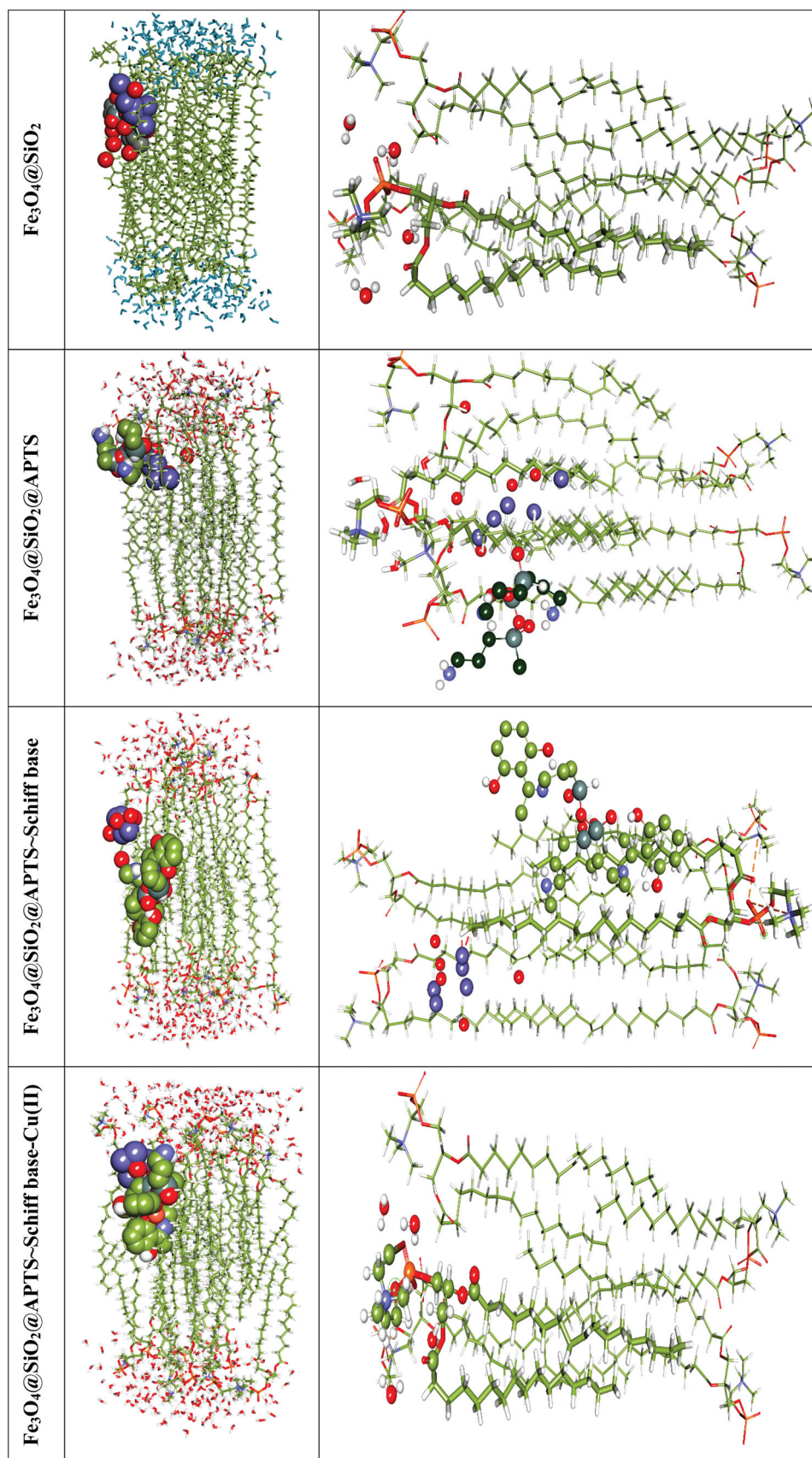


Figure 7. Docking conformation and interactions of all synthesized compounds with anionic membrane POPC.

(Malhotra & Prakash, 2011; Gholami et al., 2015). Uncoated iron oxide NPs have very low solubility which can lead to agglomeration in lungs and liver under physiological conditions and can impede blood vessels and rapidly remove macrophages leading to thromboses formation. Hence, to improve biocompatibility, dispersibility and bio-distribution, nanoparticles are coated with silica, dextran, citrate, and PEGylated starch. Functional groups of coated iron oxide NPs interact with relevant ligands and polymers to play cytotoxicity. The creation of organic molecules on iron oxide NPs surface is a fundamental step to improve structures: (i) increase stability in a pH around 7.4 and (ii) reduce adverse cellular effects. Nowadays, superparamagnetic iron oxide nanoparticles are already used medical treatments against cancer diseases and their lower systemic adverse effects were demonstrated for a long time in the human body (Hussain et al., 2005; Kim et al., 2006).

Molecular docking studies along with experimental studies could help to explore a potential drug candidate. Molecular docking simulation was carried out for all compounds with DNA, ribonucleotide reductase, and topoisomerase II. Development of novel transition-metal-based drugs which bind DNA by noncovalent modes including major and minor groove binding, electrostatic effect between the negatively charged nucleic sugar-phosphate backbone and the positive or negative end of the compounds, and intercalation is priority (Yang et al., 2017; Salehi et al., 2019). DNA topoisomerase II inhibitors such as the anthracyclines (daunorubicin and doxorubicin) bind to the transient enzyme-DNA complex and inhibit the activity of DNA Topo2 enzyme and DNA replication (Arthur, 2019). The enzyme ribonucleotide reductase as ubiquitous cytosolic enzyme catalyzes the DNA and it is one of the most important target for cancer therapy and antiviral agents in DNA synthesis, growth, metastasis, and drug resistance of cancer cells (Zaltariov et al., 2017).

The molecular docking studies of compounds showed that $\text{Fe}_3\text{O}_4@\text{SiO}_2@\text{APTS}$ strongly binds through minor groove with DNA by electrostatic and hydrogen energy (kcal/mol). In addition, the results show that the compounds $\text{Fe}_3\text{O}_4@\text{SiO}_2@\text{APTS}$ and $\text{Fe}_3\text{O}_4@\text{SiO}_2@\text{APTS} \sim \text{Schiff base-Cu(II)}$ bind strongly into topoisomerase II compared to the $\text{Fe}_3\text{O}_4@\text{SiO}_2@\text{APTS} \sim \text{Schiff base}$ and doxorubicin. The next stage, $\text{Fe}_3\text{O}_4@\text{SiO}_2@\text{APTS}$ and $\text{Fe}_3\text{O}_4@\text{SiO}_2@\text{APTS} \sim \text{Schiff base-Cu(II)}$ bind strongly into ribonucleotide reductase compared to the $\text{Fe}_3\text{O}_4@\text{SiO}_2@\text{APTS} \sim \text{Schiff base}$ and triapine. At last, $\text{Fe}_3\text{O}_4@\text{SiO}_2@\text{APTS} \sim \text{Schiff base-Cu(II)}$ binds strongly into phospholipids compared to another compounds. Over all, metal complexes as the potential anticancer drug candidates exhibited capable of binding/cleaving DNA and proteins (Gupta et al., 2013).

Disclosure statement

No potential conflict of interest was reported by the author(s).

Funding

We thank Semnan University of Medical Sciences for supporting this study.

References

- Abdesselem M, Ramodiharilafy R, Devys L, et al. (2017). Fast quantitative ROS detection based on dual-color single rare-earth nanoparticle imaging reveals signaling pathway kinetics in living cells. *Nanoscale* 9:656–65.
- Abu-Surrah AS, Kettunen M. (2006). Platinum group antitumor chemistry: design and development of new anticancer drugs complementary to cisplatin. *Curr Med Chem* 13:1337–57.
- Ankamwar B, Lai T-C, Huang J-H, et al. (2010). Biocompatibility of Fe_3O_4 nanoparticles evaluated by in vitro cytotoxicity assays using normal, glia and breast cancer cells. *Nanotechnology* 21:75102.
- Arthur DE. (2019). Molecular docking studies of some topoisomerase II inhibitors: implications in designing of novel anticancer drugs. *Radiol Infect Dis* 6:68–79.
- Halliwell B, Gutteridge JM. (2015). Free radicals in biology and medicine. USA: Oxford University Press.
- Birben E, Sahiner UM, Sackesen C, et al. (2012). Oxidative stress and antioxidant defense. *World Allergy Organ J* 5:9–19.
- Cai H, An X, Cui J, et al. (2013). Facile hydrothermal synthesis and surface functionalization of polyethyleneimine-coated iron oxide nanoparticles for biomedical applications. *ACS Appl Mater Interfaces* 5: 1722–31.
- Cai W, Yu Y, Shao X. (2006). Studies on the interaction of α -cyclodextrin with phospholipid by a flexible docking algorithm. *Chemometr Intell Lab Syst* 82:260–8.
- Chang YK, Liu YP, Ho JH, et al. (2012). Amine-surface-modified superparamagnetic iron oxide nanoparticles interfere with differentiation of human mesenchymal stem cells. *J Orthop Res* 30:1499–506.
- Chen L, Li B, Liu D. (2014). Schiff base complex coated Fe_3O_4 nanoparticles: a highly recyclable nanocatalyst for selective oxidation of alkyl aromatics. *Catal Lett* 144:1053–61.
- Choi K-H, Nam K, Cho G, et al. (2018). Enhanced photodynamic anticancer activities of multifunctional magnetic nanoparticles (Fe_3O_4) conjugated with chlorin e6 and folic acid in prostate and breast cancer cells. *Nanomaterials* 8:722.
- Dehghani F, Sardarian AR, Esmailpour M. (2013). Salen complex of Cu(II) supported on superparamagnetic $\text{Fe}_3\text{O}_4@\text{SiO}_2$ nanoparticles: an efficient and recyclable catalyst for synthesis of 1- and 5-substituted 1H-tetrazoles. *J Organomet Chem* 743:87–96.
- Di Bona KR, Xu Y, Ramirez PA, et al. (2014). Surface charge and dosage dependent potential developmental toxicity and biodistribution of iron oxide nanoparticles in pregnant CD-1 mice. *Reprod Toxicol* 50: 36–42.
- Dunford HB. (2002). Oxidations of iron (II)/(III) by hydrogen peroxide: from aquo to enzyme. *Coord Chem Rev* 233–234:311–8.
- Esmailpour M, Sardarian AR, Javidi J. (2012). Schiff base complex of metal ions supported on superparamagnetic $\text{Fe}_3\text{O}_4@\text{SiO}_2$ nanoparticles: an efficient, selective and recyclable catalyst for synthesis of 1, 1-diacetates from aldehydes under solvent-free conditions. *Appl Catal A* 445–446:359–67.
- Esmailpour M, Sardarian AR, Javidi J. (2014). Synthesis and characterization of Schiff base complex of Pd(II) supported on superparamagnetic $\text{Fe}_3\text{O}_4@\text{SiO}_2$ nanoparticles and its application as an efficient copper- and phosphine ligand-free recyclable catalyst for Sonogashira-Hagihara coupling reactions. *J Organomet Chem* 749: 233–40.
- Fahimirad B, Asghari A, Rajabi M. (2018). A novel nanoadsorbent consisting of covalently functionalized melamine onto MWCNT/ Fe_3O_4 nanoparticles for efficient microextraction of highly adverse metal ions from organic and inorganic vegetables: optimization by multivariate analysis. *J Mol Liq* 252:383–91.

- Fahimirad B, Rajabi M, Elhampour A. (2019). A rapid and simple extraction of anti-depressant drugs by effervescent salt-assisted dispersive magnetic micro solid-phase extraction method using new adsorbent $\text{Fe}_3\text{O}_4@\text{SiO}_2@\text{N}_3$. *Anal Chim Acta* 1047:275–84.
- Gholami A, Rasoul-amini S, Ebrahimezhad A, et al. (2015). Lipoamino acid coated superparamagnetic iron oxide nanoparticles concentration and time dependently enhanced growth of human hepatocarcinoma cell line (Hep-G2). *J Nanomater* 2015:1–9.
- Gupta RK, Sharma G, Pandey R, et al. (2013). DNA/protein binding, molecular docking, and in vitro anticancer activity of some thioether–dipyrinato complexes. *Inorg Chem* 52:13984–96.
- Hayashi N, Kataoka H, Yano S, et al. (2016). Anticancer effects of a new aminosugar-conjugated platinum complex agent against cisplatin-resistant gastric cancer. *Anticancer Res* 36:6005–9.
- Huang P, Li Z, Lin J, et al. (2011). Photosensitizer-conjugated magnetic nanoparticles for in vivo simultaneous magnetofluorescent imaging and targeting therapy. *Biomaterials* 32:3447–58.
- Hussain S, Hess K, Gearhart J, et al. (2005). In vitro toxicity of nanoparticles in BRL 3A rat liver cells. *Toxicol In Vitro* 19:975–83.
- Irfan A, Batool F, Zahra Naqvi SA, et al. (2020). Benzothiazole derivatives as anticancer agents. *J Enzyme Inhib Med Chem* 35:265–79.
- Jiang S, Ni H, Liu F, et al. (2020). Binuclear Schiff base copper (II) complexes: syntheses, crystal structures, HSA interaction and anti-cancer properties. *Inorg Chim Acta* 499:119186.
- Karasawa T, Steyger PS. (2015). An integrated view of cisplatin-induced nephrotoxicity and ototoxicity. *Toxicol Lett* 237:219–27.
- Karlsson HL, Cronholm P, Gustafsson J, Möller L. (2008). Copper oxide nanoparticles are highly toxic: a comparison between metal oxide nanoparticles and carbon nanotubes. *Chem Res Toxicol* 21:1726–32.
- Kim JS, Yoon T-J, Yu KN, et al. (2006). Toxicity and tissue distribution of magnetic nanoparticles in mice. *Toxicol Sci* 89:338–47.
- Kohler N, Sun C, Wang J, Zhang M. (2005). Methotrexate-modified superparamagnetic nanoparticles and their intracellular uptake into human cancer cells. *Langmuir* 21:8858–64.
- Li J, Wang X, Zheng D, et al. (2018). Cancer cell membrane-coated magnetic nanoparticles for MR/NIR fluorescence dual-modal imaging and photodynamic therapy. *Biomater Sci* 6:1834–45.
- Mahon E, Hristov DR, Dawson KA. (2012). Stabilising fluorescent silica nanoparticles against dissolution effects for biological studies. *Chem Commun (Camb)* 48:7970–2.
- Malekshah RE, Fahimirad B, Khaleghian A. (2020). Synthesis, characterization, biomedical application, molecular dynamic simulation and molecular docking of Schiff base complex of Cu(II) supported on $\text{Fe}_3\text{O}_4/\text{SiO}_2/\text{APTS}$. *Int J Nanomedicine* 15:2583–603.
- Malekshah RE, Khaleghian A. (2019). Influence of silybum marianum on morphine addicted rats, biochemical parameters and molecular simulation studies on μ -opioid receptor. *Drug Res (Stuttg)* 69:630–8.
- Malekshah RE, Salehi M, Kubicki M, Khaleghian A. (2018). New mononuclear copper (II) complexes from β -diketone and β -keto ester N-donor heterocyclic ligands: structure, bioactivity, and molecular simulation studies. *J Coord Chem* 71:952–68.
- Malekshah RE, Salehi M, Kubicki M, Khaleghian A. (2019). Biological studies and computational modeling of two new copper complexes derived from β -diketones and their nano-complexes. *J Coord Chem* 72:1697–18.
- Malekshah RE, Salehi M, Kubicki M, Khaleghian A. (2019). Synthesis, structure, computational modeling and biological activity of two new Casiopeínas[®] complexes and their nanoparticles. *J Coord Chem* 72:2233–50.
- Malhotra M, Prakash S. (2011). Targeted drug delivery across blood–brain-barrier using cell penetrating peptides tagged nanoparticles. *Curr Nanosci* 7:81–93.
- Malvindi MA, De Matteis V, Galeone A, et al. (2014). Toxicity assessment of silica coated iron oxide nanoparticles and biocompatibility improvement by surface engineering. *PLoS One* 9:e85835.
- Mancarella S, Greco V, Baldassarre F, et al. (2015). Polymer-coated magnetic nanoparticles for curcumin delivery to cancer cells. *Macromol Biosci* 15:1365–74.
- Nam KC, Choi K-H, Lee K-D, et al. (2016). Particle size dependent photodynamic anticancer activity of hematoporphyrin-conjugated Fe_3O_4 particles. *J Nanomater* 2016:1–9.
- Niemirowicz K, Prokop I, Wilczewska AZ, et al. (2015). Magnetic nanoparticles enhance the anticancer activity of cathelicidin LL-37 peptide against colon cancer cells. *Int J Nanomedicine* 10:3843–53.
- Nigam S, Bahadur D. (2016). Dendrimerized magnetic nanoparticles as carriers for the anticancer compound, epigallocatechin gallate. *IEEE Trans Magn* 52:1–5.
- Palmieri B, Sblendorio V. (2007). Oxidative stress tests: overview on reliability and use. *Eur Rev Med Pharmacol Sci* 11:383–99.
- Rabik CA, Dolan ME. (2007). Molecular mechanisms of resistance and toxicity associated with platinating agents. *Cancer Treat Rev* 33:9–23.
- Ranmadugala D, Ebrahimezhad A, Manley-Harris M, et al. (2017). Impact of 3-aminopropyltriethoxysilane-coated iron oxide nanoparticles on menaquinone-7 production using *B. subtilis*. *Nanomaterials* 7:350.
- Revathi N, Sankarganesh M, Dhaweethu Raja J, et al. (2020). Bio-active mixed ligand Cu(II) and Zn(II) complexes of pyrimidine derivative Schiff base: DFT calculation, antimicrobial, antioxidant, DNA binding, anticancer and molecular docking studies. *J Biomol Struct Dyn* 1–13.
- Roobzahani P, Salehi M, Malekshah RE, Kubicki M. (2019). Synthesis, crystal structure, electrochemical behavior and docking molecular of poly-nuclear metal complexes of Schiff base ligand derived from 2-amino benzyl alcohol. *Inorg Chim Acta* 496:119022.
- Salehi M, Kubicki M, Galini M, et al. (2019). Synthesis, characterization and crystal structures of two novel sulfa drug Schiff base ligands derived sulfonamide and molecular docking study. *J Mol Struct* 1180:595–602.
- Shen M, Cai H, Wang X, et al. (2012). Facile one-pot preparation, surface functionalization, and toxicity assay of APTS-coated iron oxide nanoparticles. *Nanotechnology* 23:105601.
- Singh N, Jenkins GJ, Asadi R, Doak SH. (2010). Potential toxicity of superparamagnetic iron oxide nanoparticles (SPION). *Nano Rev* 1:5358.
- Tavassoli M, Montazerzohori M, Naghiha R, et al. (2020). Some new nanostructure zinc complex: synthesis, spectral analyses, crystal structure, Hirshfeld surface analyses, antimicrobial/anticancer, thermal behavior and usage as precursor for ZnO nanostructure. *Mater Sci Eng C Mater Biol Appl* 110:110642.
- Voinov MA, Sosa Pagán JO, Morrison E, et al. (2011). Surface-mediated production of hydroxyl radicals as a mechanism of iron oxide nanoparticle biotoxicity. *J Am Chem Soc* 133:35–41.
- Yang H, Tang P, Tang B, et al. (2017). Studies of DNA-binding properties of lafutidine as adjuvant anticancer agent to calf thymus DNA using multi-spectroscopic approaches, NMR relaxation data, molecular docking and dynamical simulation. *Int J Biol Macromol* 99:79–87.
- Yilmaz VT, Icel S, Suyunova F, et al. (2016). Ni(ii)/Cu(ii)/Zn(ii) 5,5-diethylbarbiturate complexes with 1,10-phenanthroline and 2,2'-dipyridylamine: synthesis, structures, DNA/BSA binding, nuclease activity, molecular docking, cellular uptake, cytotoxicity and the mode of cell death. *Dalton Trans* 45:10466–79.
- Yin M, Li Z, Liu Z, et al. (2012). Photosensitizer-incorporated G-quadruplex DNA-functionalized magnetofluorescent nanoparticles for targeted magnetic resonance/fluorescence multimodal imaging and subsequent photodynamic therapy of cancer. *Chem Commun (Camb)* 48:6556–8.
- Zaltariov MF, Hammerstad M, Arabshahi HJ, et al. (2017). New iminodiacetate-thiosemicarbazone hybrids and their copper(II) complexes are potential ribonucleotide reductase R2 inhibitors with high antiproliferative activity. *Inorg Chem* 56:3532–49.
- Zhao X, Chen Z, Zhao H, et al. (2014). Multifunctional magnetic nanoparticles for simultaneous cancer near-infrared imaging and targeting photodynamic therapy. *RSC Adv* 4:62153–9.